CrossMark

Unexpected Behavior of the Solar Wind Mass Flux During Solar Maxima: Two Peaks at Middle Heliolatitudes

Olga Katushkina[1] · Vladislav Izmodenov[1,2,3] ·
Dimitra Koutroumpa[4] · Eric Quémerais[4] · Lan K. Jian[5]

Abstract In this work we study the temporal and latitudinal variations of the solar wind mass flux at 1 AU derived from SOHO/SWAN data on backscattered solar Lyman-α radiation in 1996 – 2018. Previously Katushkina *et al.* (*J. Geophys. Res.* **118**, 2800, 2013) have shown that the latitudinal profiles of the solar wind mass flux during the solar maximum 2001 – 2003 have two separate peaks at middle heliolatitudes. In this work we provide the data for the last solar maximum in 2014 – 2016 and show that the specific latitudinal distribution appears again. However, in 2014 – 2016 the two peaks are less separated and sometimes merged to one peak. For several years we have performed a comparison of SWAN observations with the results of the WSA-Enlil model, which is a coupled 3D time-dependent model of the solar wind propagation from the solar corona to the heliosphere. It is shown that the WSA-Enlil model confirms qualitatively the latitudinal distribution of the solar wind found from the SWAN data, although there are some quantitative differences. Physical reasons for the formation of this latitudinal structure at the solar maxima are discussed. Further investigation is needed and could provide new links between the solar corona and the heliospheric environment.

This article belongs to the Topical Collection:
Solar Wind at the Dawn of the Parker Solar Probe and Solar Orbiter Era
Guest Editors: Giovanni Lapenta and Andrei Zhukov

✉ O. Katushkina
okat@iki.rssi.ru

[1] Space Research Institute of Russian Academy of Sciences, Profsoyuznaya Str. 84/32, Moscow, 117335, Russia

[2] Lomonosov Moscow State University, GSP-1, Leninskie Gory, Moscow, 119991, Russia

[3] Ishlinsky Institute for Problems in Mechanics of Russian Academy of Sciences, Moscow, 119526, Russia

[4] Université Versailles Saint-Quentin, LATMOS, Guyancourt, France

[5] Heliophysics Science Division, NASA Goddard Space Flight Center, Greenbelt, MD, USA

1. Introduction

The solar wind as a phenomenon of supersonic expansion of the solar corona was predicted theoretically by Parker (1958) and then it was observed at the very beginning of the space era (Gringauz *et al.*, 1960; Neugebauer and Snyder, 1962). The solar wind originates in the solar corona and, therefore, its parameters *e.g.* at 1 AU characterize the physical nature of the solar atmosphere expansion and acceleration. On the other side, the solar wind propagates far away from the Sun and interacts with the interstellar medium at the heliospheric boundary. In other words, the solar wind is a link between the solar corona and the outer regions of the solar system.

Information about the three-dimensional (3D) structure and temporal evolution of the solar wind parameters is necessary and important for many different branches of space science such as solar physics, space weather forecasting, and modeling of the inner and outer heliosphere and beyond. For many decades the solar wind parameters have been measured in the ecliptic plane (mostly at the Earth orbit) and collected by the OMNIWeb database (https://omniweb.gsfc.nasa.gov, King and Papitashvili, 2005). The only spacecraft that carried out *in situ* routine measurements out of the ecliptic plane was *Ulysses* operating in 1990 – 2010 (McComas, 2003; McComas *et al.*, 2006, 2008). The *Ulysses* data provide unique information on the heliolatitudinal variations of the solar wind parameters during nearly two solar cycles. It was shown that at solar minimum the solar wind has a distinct latitudinal structure, namely, it is dense and slow near the solar equator and rarefied and fast near the poles (McComas *et al.*, 2000). At the solar maximum situation it is much more complex; fast and slow solar wind flows are mixed and an irregular latitudinal structure appears (McComas *et al.*, 2002; McComas, 2003).

Although the *Ulysses* data are unique and give the first view of the 3D structure of the solar wind over the solar cycle, these data are insufficient for the reconstruction of the global temporal and heliolatitudinal variations of the solar wind. Local *in situ* measurements allow one to gather information only along the spacecraft's trajectory, while for many problems it is necessary to know what happens at all latitudes simultaneously. There are several indirect methods of remote diagnostic of the solar wind that help to reconstruct the solar wind parameters at different latitudes at the same time.

One important method for remote sensing of the solar wind is interplanetary scintillation (IPS) observations. This method is based on the idea that radio waves generated by remote compact objects (like quasars) are scattered by density fluctuations in the solar wind. And the level of electron density fluctuations is correlated with the solar wind velocity. Tomographic methods are used to reconstruct the solar wind speed and its latitudinal variations (see *e.g.* Tokumaru, Kojima, and Fujiki, 2012). Another method deals with deriving the 3D electron coronal density distribution from measurements of Thomson-scattered brightness by coronographs (Quémerais and Lamy, 2002; Kramar *et al.*, 2009; Kramar, Airapetian, and Lin, 2016). This method allows one to obtain the temporal and heliolatitudinal distribution of the solar wind electron number density at a distance of several (2 – 4) solar radii. Still another method is based on Doppler dimming technique applied for an analysis of the solar Lyman-α and polarized brightness images from the *Ultraviolet Coronagraph Spectrometer* (UVCS) and the *Large Angle and Spectrometric Coronagraph* (LASCO-C2) on board the *Solar and Heliospheric Observatory* (SOHO) (Bemporad, 2017). This method provides 2D maps of the radial solar wind velocity and density between 1 to 6 solar radii.

In this paper we are focused on a fourth method of the remote diagnostic of the solar wind mass flux. This method is based on the measurements of heliospheric backscattered

Lyman-α intensities performed by the instrument *Solar Wind ANisotropy* (SWAN) onboard SOHO (Bertaux *et al.*, 1995). Backscattered Lyman-α radiation comes from interstellar hydrogen (H) atoms penetrating the heliosphere from the interstellar medium. The intensity of this radiation depends on the number density of H atoms, which, in turn, depends on the hydrogen ionization rate in the heliosphere. The main ionization process is charge exchange of H atoms with the solar wind protons, and the charge exchange ionization rate depends on the solar wind mass flux following $\beta_{ex}(t, \mathbf{r}) \approx n_{\mathrm{sw}}(t, \mathbf{r}) \cdot v_{\mathrm{sw}}(t, \mathbf{r}) \cdot \sigma_{\mathrm{ex}}(v_{\mathrm{sw}})$, where n_{sw} and v_{sw} are the solar wind number density and velocity. Generally speaking, the charge exchange cross-section σ_{ex} depends on the relative velocity between the hydrogen atom and the solar wind proton. However, the typical velocity of the supersonic solar wind is about $400 - 700$ km s^{-1}, while the typical velocity of the interstellar hydrogen atoms in the heliosphere is about 20 km s^{-1}, therefore it can be assumed that the relative velocity is equal to the solar wind velocity. Due to a weak dependence of σ_{ex} on v_{sw} (Lindsay and Stebbings, 2005) it is possible to say that the charge exchange ionization rate is proportional to the solar wind mass flux.

Therefore, the Lyman-α intensities measured by SWAN at the Earth orbit depend on spatial and temporal distribution of the solar wind mass flux. It is possible to use full-sky maps of the backscattered Lyman-α radiation for remote sensing of temporal and latitudinal variations of the solar wind parameters. The inversion procedure is described in detail by Quémerais *et al.* (2006) and was applied before by Lallement *et al.* (2010) and Katushkina *et al.* (2013).

Katushkina *et al.* (2013) have shown that at the solar minima $1996 - 1997$ and $2009 - 2010$ the latitudinal variations of the charge exchange ionization rate derived from SWAN data follow the typical behavior of the solar wind number density, namely, it has a maximum near the solar equator (or ecliptic) plane and minima at the poles. However, near the solar maximum $2002 - 2005$ the charge exchange ionization rate obtained from the SWAN data has two separated maxima at middle latitudes ($\pm 30 - 50°$). These maxima were not observed by *Ulysses*, because its trajectory passed between them. The physical nature of these maxima was not known and it remained a question whether they would appear again during the new solar maximum $2014 - 2016$ or not.

Section 2.1 of this paper presents the charge exchange ionization rate obtained from the SWAN data for the whole period of observations ($1996 - 2018$). It is shown that in $2014 - 2016$ two maxima of the charge exchange ionization rate are seen again, but sometimes they are less distinguishable and merged together. Also for certain years we perform a comparison of β_{ex} derived from SWAN data with the results of 3D time-dependent model of the solar wind, namely, we use the Wang–Sheely–Arge (WSA) Enlil model installed at the Community Coordinated Modeling Center (CCMC). The results of the comparison are presented in Section 2.2. A numerical modeling of the Lyman-α intensity maps based on both SWAN and WSA-Enlil latitudinal variations of the ionization rates is performed in Section 3 and compared with the SWAN data.

2. Temporal and Latitudinal Variations of the Charge Exchange Ionization Rate of Hydrogen at 1 AU

In this section we present 2D (time–latitude) maps of the charge exchange ionization rate obtained from the SWAN Lyman-α data and compare them with the WSA-Enlil model results.

SWAN Lyman-α intensity maps
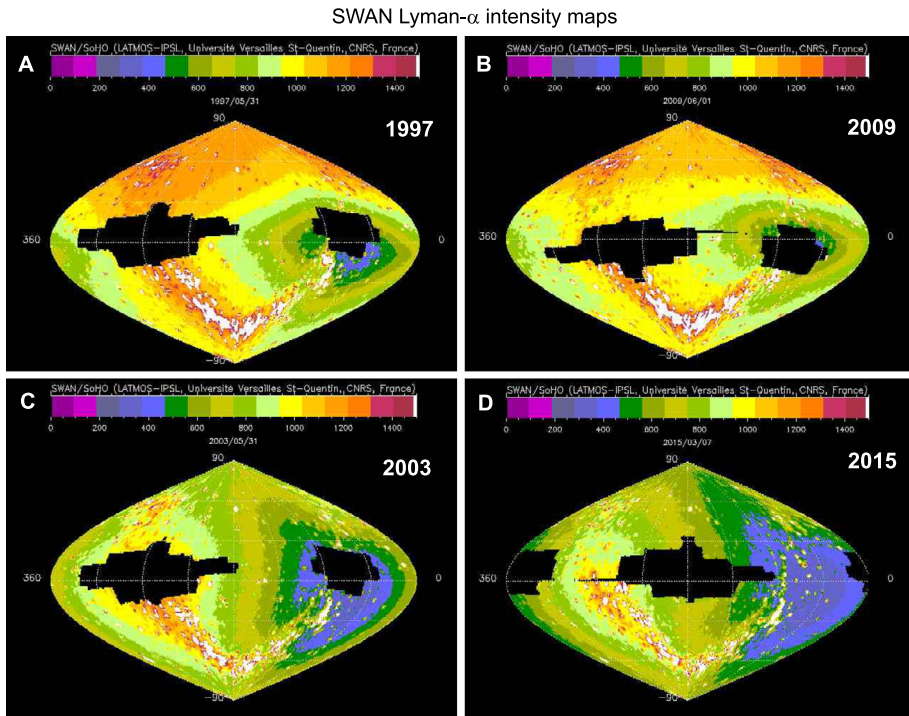
Figure 1 SOHO/SWAN data are available at the web-site http://swan.projet.latmos.ipsl.fr. Four examples of full-sky intensity maps of the backscattered solar Lyman-α radiation at the solar minima (1997, 2009) and the solar maxima (2003, 2015) are presented.

2.1. From Lyman-α Intensity Maps to the Charge Exchange Ionization Rate

Figure 1 presents the full-sky maps of the Lyman-α intensities obtained by SOHO/SWAN during solar minima (1997 and 2009) and solar maxima (2003 and 2015). Intensity of backscattered solar Lyman-α emission is an integral along the line of sight (LOS) and, roughly speaking, characterizes the amount of H atoms along the LOS. More H atoms produce larger intensity of backscattered radiation. It is seen from Figure 1 that the shapes of the maps are different at solar maximum and minimum. Namely, at solar minima, the maximum of intensity is located around the north ecliptic pole, while at solar maxima, the intensity maximum is close to the upwind direction, which is the direction of the Sun's motion through the local interstellar medium (its ecliptic J2000 longitude is about 255.4° and north ecliptic latitude is about 5.2°; see Lallement *et al.*, 2010). The minimum of the intensity for all years is located close to the opposite downwind direction, which corresponds to the tail of the heliosphere, where only a small number of H atoms survive. Joselyn and Holzer (1975) have shown for the first time that the shape of the Lyman-α intensity map depends on the heliolatitudinal profile of the hydrogen charge exchange ionization rate. It was confirmed later by other authors, *e.g.*, Lallement, Bertaux, and Kurt (1985a) and Katushkina *et al.* (2013). Therefore different distributions in the intensity maps suggest that the latitudinal dependences of the charge exchange ionization rate at solar maximum and minimum are different.

    Quémerais *et al.* (2006) have developed the inversion algorithm for deriving the total ionization rate $\beta_{\text{tot}}^{\text{swan}}(t_0, \lambda)$ at 1 AU from the Sun for each certain full-sky SWAN intensity
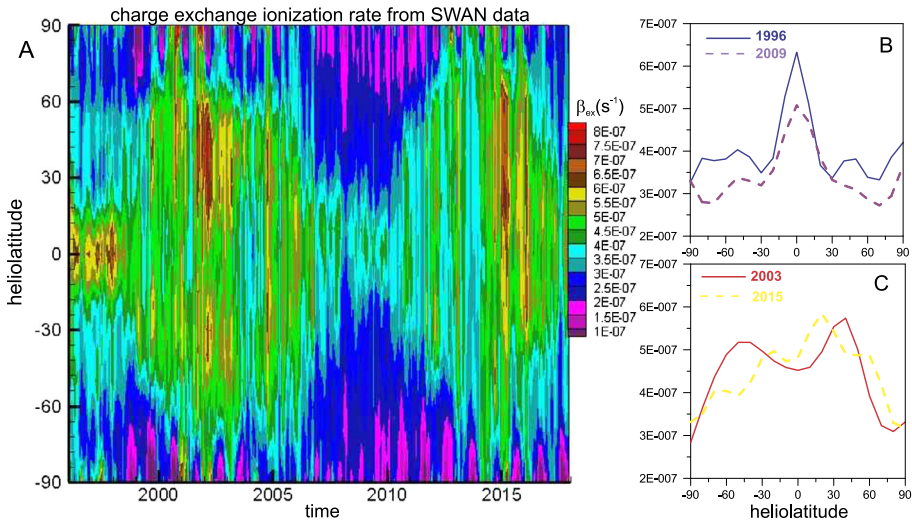
Figure 2 **A**. Temporal and latitudinal variations of the charge exchange ionization rate derived from SWAN data. Plots **B** and **C** show 1D slices of latitudinal profiles in the middle of each year. Plot **B** corresponds to the solar minimum periods (years 1996, 2009), plot **C** corresponds to the solar maximum (years 2003, 2015).

map obtained at time moment t_0 (λ is the heliolatitude). The total ionization rate is a sum of the charge exchange ionization rate (the major component) and the photoionization rate (the minor component). To do this it was assumed that both ionization rates fall with the heliocentric distance as $\sim 1/r^2$. The latitudinal resolution of the results is 10 degree, the temporal resolution depends on the observational frequency of SWAN, which is about $2-3$ times per week in $1996-2007$ and about once per day since 2008. We applied this procedure for the whole period of SWAN observations in $1996-2018$. As was done before in Katushkina *et al.* (2013) we normalized the ionization rates from SWAN to the *in situ* OMNI data in solar ecliptic plane by the following:

$$\beta_{\mathrm{ex}}(t, \lambda) = \beta_{\mathrm{ex}}^{\mathrm{omni}}(t) \cdot \frac{\beta_{\mathrm{tot}}^{\mathrm{swan}}(t, \lambda)}{\beta_{\mathrm{tot}}^{\mathrm{swan}}(t, 0°)},$$

and averaged the results over one Carrington rotation (~ 27 days). Here, $\beta_{\mathrm{ex}}^{\mathrm{omni}}(t)$ is the charge exchange ionization rate at 1 AU obtained from the OMNI *in situ* data. The obtained charge exchange ionization rate is shown in Figure 2A. It is seen that during the solar minima of 1996 and 2009 the latitudinal variations of the charge exchange ionization rate are predicted with one distinct maximum at zero latitude (the same is shown by 1D slices in Figure 2B). During the solar maxima of 2003 and 2015 there is a structure with characteristic features at middle latitudes: namely, there are two separated maxima in 2003, while they seem to be merged in 2015 (1D slices are presented in Figure 2C).

2.2. Comparison with WSA-Enlil Model Results from CCMC

In order to better understand the physical reasons of the observed specific latitudinal variations of the solar wind parameters we decided to perform direct calculations of $n(t, \mathbf{r})$ and $v(t, \mathbf{r})$ in the frame of a time-dependent 3D MHD model of the solar wind propagation
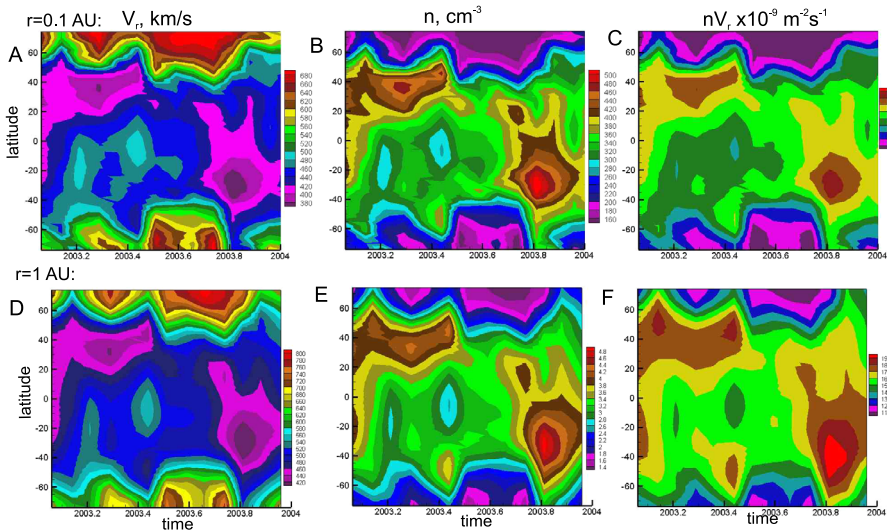
Figure 3 2D maps of the solar wind parameters (radial velocity, number density and mass flux) based on the WSA-Enlil model run in 2003. All parameters are averaged over longitude and are presented as functions of time and heliolatitude. Plots **A–C** correspond to the inner boundary conditions of the Enlil model at 0.1 AU, plots **D–F** correspond to the model results obtained at 1 AU.

from the solar corona to the heliosphere. We use the WSA-Enlil model available for runs on request at the web-site of the Community Coordinated Modeling Center.

The WSA coronal model uses synoptic magnetograms as input, combines a Potential-Field Source Surface model with the Schatten current sheet model to produce a global magnetic field configuration at 21.5 solar radii (R_s) that is about 0.1 AU, and uses an improved Wang and Sheeley empirical relationship to derive the solar wind speed at this distance (*e.g.*, Arge and Pizzo, 2000; Arge *et al.*, 2003). After that the solar wind number density at 21.5 R_s is taken from the assumption that the solar wind dynamical pressure ($n \cdot V^2$) is constant over time, latitude and longitude (Odstrcil, 2003). This assumption is based on the analysis of *Mariner 2* and *Helios 1* data (see, *e.g.*, Steinitz and Eyni, 1980). Obtained in this way, the solar wind parameters at 0.1 AU are used as the inner boundary conditions for the Enlil model (the distributions of radial velocity V_r, number density n and mass flux nV_r are presented in Figure 3A–C). The Enlil model propagates the solar wind outward to an adjustable heliocentric distance (typically $1 - 10$ AU), based on the MHD equations (*e.g.*, Odstrcil, 2003; Pizzo *et al.*, 2011).

The coupled WSA v2.2 and Enlil v2.8 models are executed for three years: 2003 (close to solar maximum), 2007 (close to solar minimum) and 2014 (close to solar maximum). The integral Carrington rotation synoptic magnetograms from the *Global Oscillation Network Group* (GONG) were used as the input of the WSA-Enlil model for 2007 and 2014. For the 2003 calculations we switched to using the integral Carrington rotation synoptic magnetograms from the National Solar Observatory (NSO) *Synoptic Optical Long-term Investigations of the Sun* (SOLIS) as the input, because GONG synoptic magnetograms were not available to run for 2003. The use of different synoptic magnetograms would introduce some discrepancy in the simulation results (Jian *et al.*, 2015, 2016), but it would not greatly affect the large-scale structure and the general trend which are under investigation in this study.
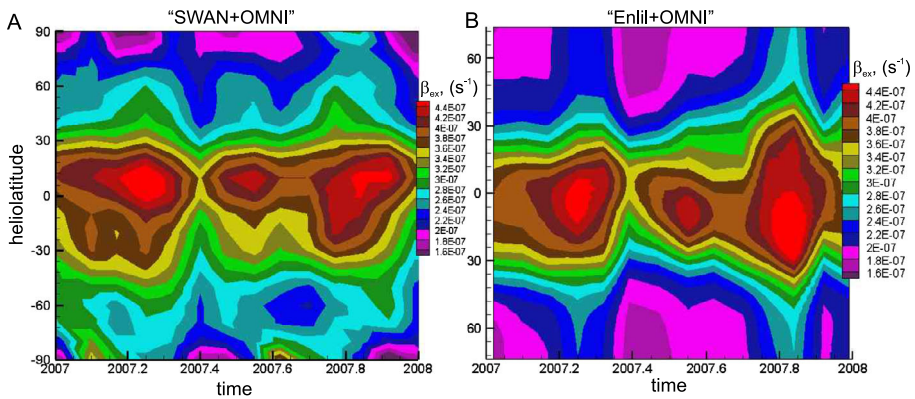
Figure 4 2D maps of the charge exchange ionization rate in 2007. Plot **A** presents β_{ex}-values found from SWAN Lyman-α intensity maps. Plot **B** presents β_{ex}-values obtained from the WSA-Enlil model results. Both datasets are normalized to *in situ* OMNI data in the solar ecliptic plane.

From this modeling system we get n and $\mathbf{V}$ at a sphere with radius 1 AU, with $4°$-resolution in latitude (up to $\pm 74°$) and longitude and temporal resolution of one Carrington rotation for each chosen year. Based on these data we calculate the charge exchange ionization rate β_{ex}^{enlil}. Then we average the results over longitude and normalize to the OMNI data in the ecliptic plane (as we do before for β_{ex}^{swan} obtained from SWAN observations). Figure 3D–F presents the solar wind parameters (V_r, n, nV_r) obtained at 1 AU (after averaging over longitude) in 2003.

Thus we have two sets of charge exchange ionization rates, $\beta_{ex}^{swan}(t, \lambda)$ and $\beta_{ex}^{enlil}(t, \lambda)$, for the three chosen years. The two sets of the data have the same temporal resolution and are normalized to the OMNI data in the ecliptic plane. Figure 4 shows a comparison between two datasets at the solar minimum of 2007. It is seen that the data agree with each other and show one maximum of the charge exchange ionization rate at zero heliolatitude as predicted for the solar minimum conditions.

Figures 5 and 6 show a comparison of two β_{ex}-datasets for 2003 and 2014 years, respectively. It is seen that in 2003 WSA-Enlil model also predicts two maxima of the charge exchange ionization rate at middle latitudes in agreement with the SWAN data. In 2014 local 1D latitudinal profiles agree less, but a general sample of latitudinal distribution of β_{ex} is similar for two datasets. This means that the characteristic features of latitudinal distribution of the solar wind mass flux obtained from the SWAN data during solar maxima have some physical basis, which are involved in the WSA-Enlil model. From comparison of the distributions at 0.1 and 1 AU shown in Figure 3 it is seen that latitudinal variations of the solar wind number density, velocity and mass flux are qualitatively the same at the inner boundary (0.1 AU) and at 1 AU. This means that the latitudinal structure of the charge exchange ionization rate obtained in the Enlil model at 1 AU is determined by the boundary conditions posed at 0.1 AU. In Section 4 we discuss some possible reasons for the formation of such structures close to the Sun.

3. Numerical Modeling of Lyman-α Intensity Maps

In this section we perform a numerical modeling of the Lyman-α intensity maps with input β_{ex} from both datasets and compare the results with SWAN maps. In our calculations we use
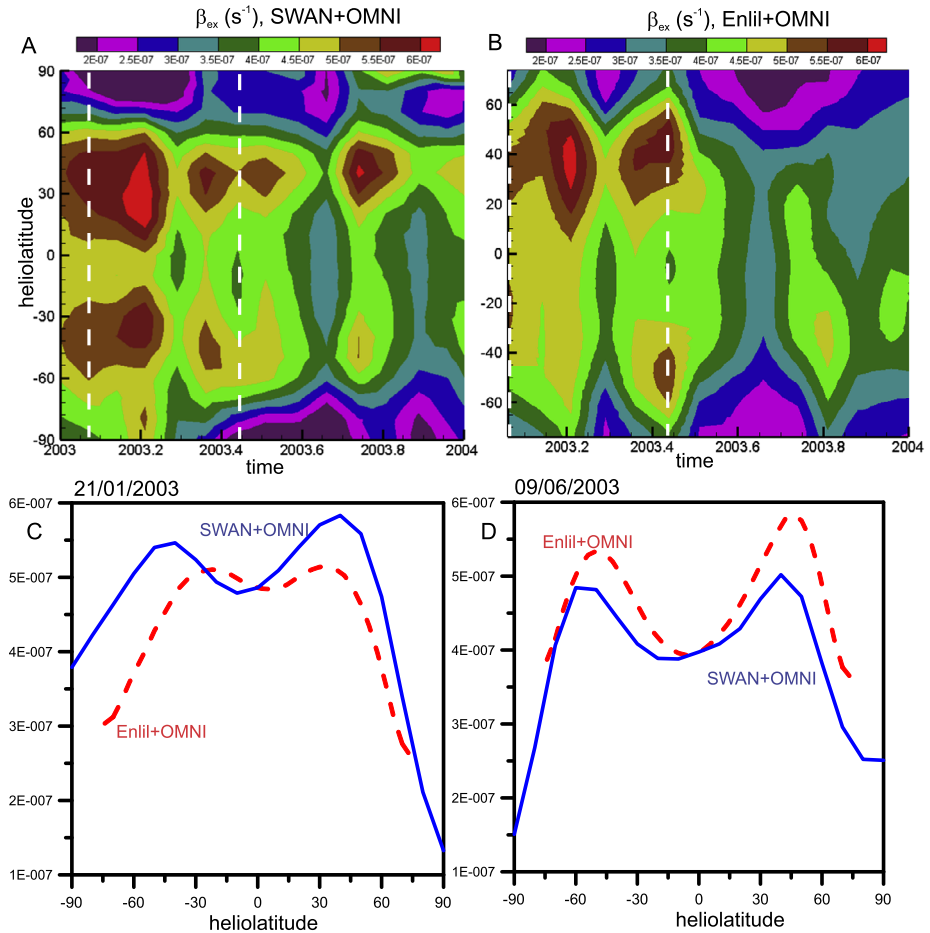
Figure 5 Plots **A** and **B** are the same as in Figure 4 for the year 2003. Plots **C** and **D** present 1D slices of latitudinal profiles at certain moments of time (marked with *dashed white lines* in Plots **A–B**) for a comparison between two datasets.

a 3D quasi-stationary kinetic model of the hydrogen distribution in the heliosphere (Izmode-nov *et al.*, 2013; Katushkina *et al.*, 2015). The model is an analog of the classical hot model (Meier, 1977; Wu and Judge, 1979; Lallement, Bertaux, and Dalaudier, 1985b), but it takes into account disturbances of the H distribution in the interaction region of the solar wind with the interstellar medium. The kinetic equation for the hydrogen velocity distribution function is solved at distances less than 90 AU from the Sun, and the boundary conditions at a sphere with radius 90 AU are based on the results of a 3D kinetic-MHD model of the heliosphere and its boundary (Izmodenov and Alexashov, 2015). We use a quasi-stationary version of the model, because, as it was shown by Katushkina *et al.* (2013), such a model allows one to qualitatively reproduce the Lyman-α intensity map quite well. The charge ex-change ionization rate as a function of heliolatitude is the input parameter of the model. We take it from both "SWAN+OMNI" and "Enlil+OMNI" datasets ("+OMNI" means that the data are normalized to OMNI values in the ecliptic plane). To calculate the intensities of the backscattered Lyman-α radiation with the known hydrogen velocity distribution function in
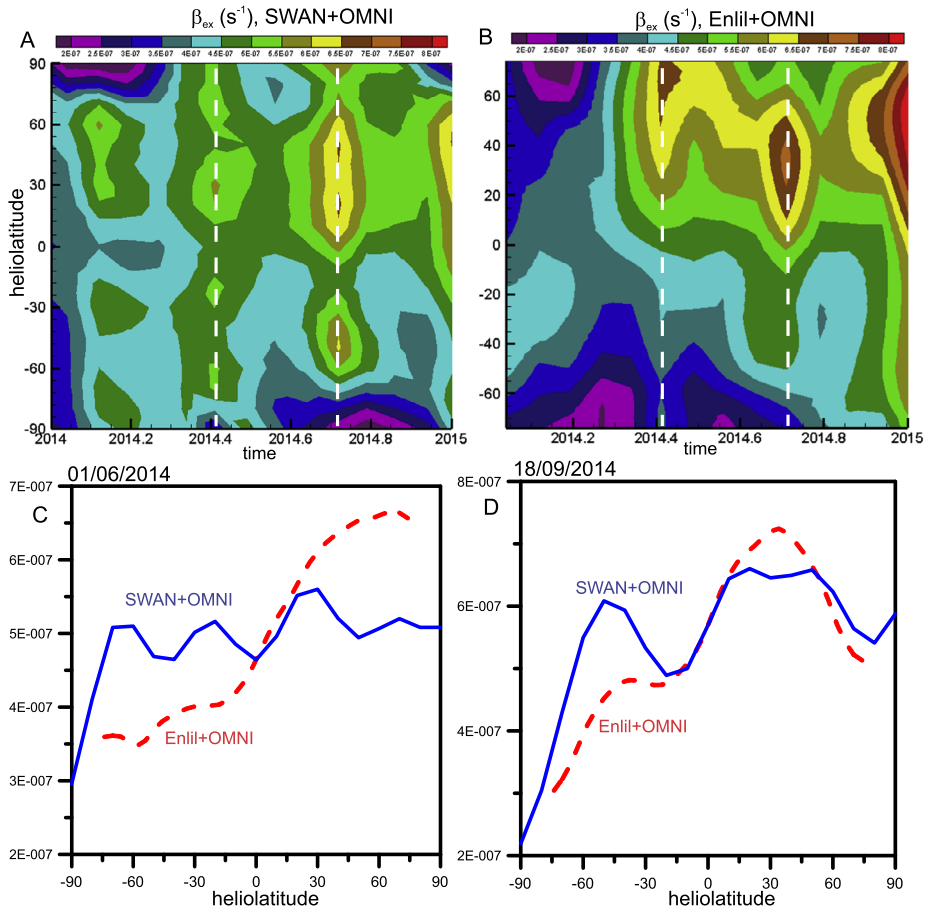
Figure 6 The same as Figure 5 for the year 2014.

the heliosphere we use the so-called "self-absorption" approximation (see Quémerais and Izmodenov, 2002). In this case multiple scattering of photons is neglected, but the difference with an optically thin approach is that the extinction between the scattering point and the observer is taken onto account. Quémerais and Izmodenov (2002) have shown that the upwind-to-downwind ratio of the Lyman-α intensities obtained in the model under the self-absorption approximation agrees well with the full radiative transfer calculations. Here we only qualitatively analyze the maps (we are not interested in absolute values of intensities), therefore, this approach is appropriate for our goals. Calculations are performed for two distinct dates: June, 1 in 2003 and June, 1 in 2014. At these dates (beginning of June each year) Earth was located close to the upwind direction related to the Sun.

Figure 7 presents the results of the modeling and comparison with the SWAN data. All intensities are normalized to the intensity in one direction between upwind and downwind. It is seen that results with input β_{ex} from SWAN agree with the data very well. This is not surprising of course. But it should be noted that the inversion algorithm for deriving β-values from the SWAN data is based on the classical hot model and is independent from our numerical kinetic model of H distribution in the heliosphere. Good agreement between our
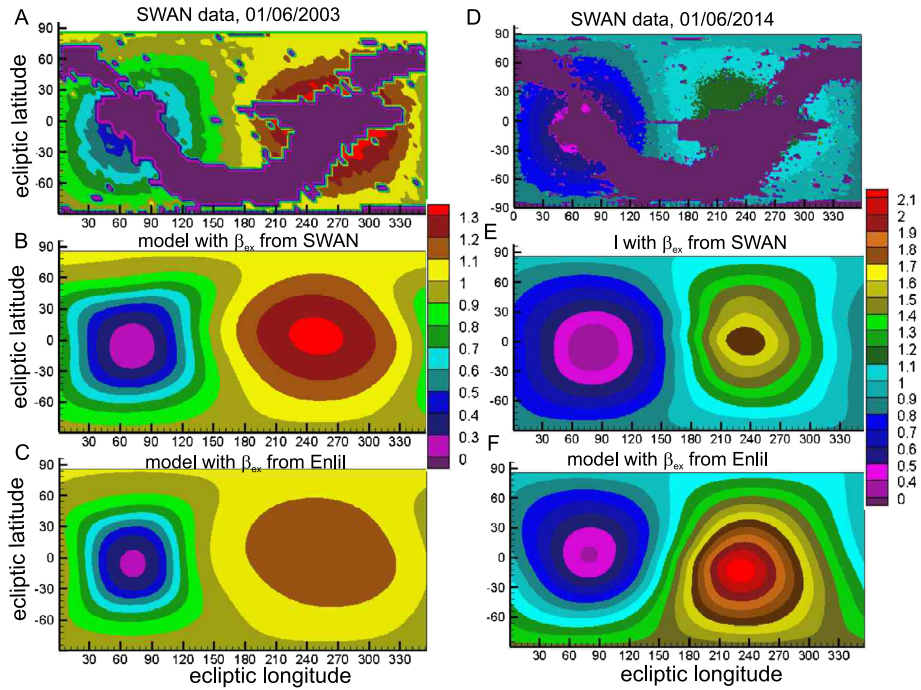
Figure 7 Results of the numerical modeling of Lyman-α intensity maps (in J2000 ecliptic coordinates) and a comparison with SWAN data for June 1st in 2003 (**A**–**C**) and 2014 (**D**–**F**). Intensities from each map are normalized to corresponding intensity at chosen direction (with ecliptic longitude 160.5° and ecliptic latitude 70.5°). Plots **A** and **D** present SWAN data. Plots **B** and **E** present the results of numerical model with input parameter β_{ex} taken from the inversion procedure of SWAN data (Quémerais *et al.*, 2006). Plots **C** and **F** present the results of numerical model with input parameter β_{ex} taken from the WSA-Enlil model.

modeling and the data means that the models are consistent with each other and the inversion procedure works well. Model results with input β_{ex} from the WSA-Enlil model agree with the SWAN data qualitatively, although the quantitative differences are significant as seen from Figure 7. Studying the reasons of these quantitative differences requires a much more detailed analysis, which is beyond the scope of this paper. For us it is important to note that the shapes of the Lyman-α intensity maps obtained by the model with input β_{ex} from the WSA-Enlil model results agree with the SWAN data for both 2003 and 2014.

4. Discussion and Conclusions

In this paper we present the temporal and latitudinal variations of the charge exchange ionization rate at 1 AU derived from SOHO/SWAN full-sky maps of the backscattered solar Lyman-α radiation in 1996 – 2018. Let us recall that the charge exchange ionization rate is proportional to the solar wind mass flux; therefore its variations represent variations of the solar wind mass flux. It is shown that the characteristic structure with two maxima of β_{ex} at middle latitudes during the solar maximum of 2001 – 2003 discovered before by SWAN appears again at the latest solar maximum 2014 – 2016. However, these two maxima of β_{ex} in 2014 – 2016 are located closer to the solar equator plane and less separated from each

other, at some time moments they are merged to one maximum. This can be partly due to the weaker solar activity in Cycle 24 than in Cycle 23 (McComas *et al.*, 2013).

We perform a comparison of β_{ex} from SWAN with the results of the WSA-Enlil model of the solar wind in 2003, 2007 and 2014. It is shown that in 2007 (near solar minimum) both datasets agree with each other very well. In 2003 the WSA-Enlil model also shows two maxima of β_{ex}, and in general the qualitative agreement with the SWAN results is quite good. In 2014 the differences between the two datasets are the largest, but still, there is a qualitative agreement in the general latitudinal structure. Numerical modeling of the Lyman-α intensity maps with input β_{ex} taken from the WSA-Enlil model results shows qualitative agreement with the SWAN data. Therefore we can conclude that the surprising latitudinal behavior of the solar wind mass flux (which is proportional to β_{ex}) discovered by SWAN during solar maxima is qualitatively confirmed by the WSA-Enlil model results. But the reason for the formation of this structure is still an open question. Let us consider several observational and theoretical issues, which could help to clarify the point.

Lamy *et al.* (2017) displays the heliolatitudinal distribution of the coronal electron density at a heliocentric distance of 3.5 solar radii computed by inversion of the LASCO white light coronal images as described by Lamy *et al.* (2014). They compare the results with the solar wind mass flux derived from the SWAN data in 1996 – 2014 (see Figure 8 in Lamy *et al.*, 2017) and showed the qualitative similarity of the distributions.

Generally speaking, the latitudinal structure of the charge exchange ionization rate obtained from the SWAN data is similar to a classical butterfly diagram of sunspot area. Sunspots concentrate at middle latitudes at the beginning of each solar cycle, then they move through the low latitudes at solar maximum, reach the equator and then disappear at solar minimum. The spatial distribution of sunspots correlates with the distribution of the solar flares and coronal mass ejections (CMEs) as shown, *e.g.*, by McIntosh *et al.* (2015). Therefore, it can be supposed that the latitudinal distribution of the solar wind mass flux at solar maxima is connected with the distribution of the coronal holes, active regions on the Sun's surface and CMEs (see, *e.g.*, Ebert *et al.*, 2009; Lamy *et al.*, 2017). It is well known from different observations that the solar wind number density anticorrelates with velocity (Neugebauer and Snyder, 1966; Hundhausen *et al.*, 1970; Steinitz and Eyni, 1980; McComas *et al.*, 2000). Let us recall that at the inner boundary of the Enlil model it is assumed that the dynamical pressure (nV^2) is constant, which means that the larger solar wind velocity corresponds to the smaller mass flux (nV) and *vice versa*. This relation imposes conditions on the large-scale mass flux distribution well out into the heliosphere, although our calculations show that at 1 AU the solar wind dynamic pressure in the Enlil model results varies with latitude by about $20-30\%$. The fast and rarefied solar wind originates from coronal holes that are mostly located at poles, while the slow and dense solar wind originates from the streamer belt, which is located near the solar equator at solar minimum and expands toward the poles at solar maximum. Therefore at solar minimum the solar wind velocity has a minimum at the equator and maxima at poles, while the solar wind mass flux as expected has a maximum at the equator and minima at poles. At solar maxima the streamer belt expands toward the poles and some equatorial coronal holes may occur (Lowder, Qiu, and Leamon, 2017) at low latitudes, which leads to shift of the velocity's decrease (and corresponding increase of the mass flux) to the middle latitudes as it is seen in the SWAN data and WSA-Enlil model results.

In principle, we can conclude that the SWAN data confirms that the basic assumption of $nV^2 = $ const built into the Enlil model indeed has a physical basis. Steinitz (1983) and Bruno *et al.* (1986) have analyzed the *Helios 1* and *2* data obtained as close as 0.3 AU to the Sun and showed that the solar wind dynamic pressure (nV^2) is constant over $\pm 25°$ latitudinal

range. Schwenn ([2006](#)) commented on this finding: "There is no explanation yet for these strange invariances. We have reasons to suspect that a crucial clue to the understanding of the solar wind phenomenon may be hidden here." McComas *et al.* ([2000](#)) have analyzed the first full polar orbit of the *Ulysses* spacecraft and reported that the dynamic flux changes a bit over latitudes. It could be caused by the fact that *Ulysses* performed measurements further than 1 AU from the Sun, where different solar wind flows may be mixed up and initial invariants may be changed. McComas *et al.* ([2006](#), [2008](#)) have reported the *Ulysses* data obtained during the second and third orbit and showed that the solar wind dynamic pressure is more or less constant over time and latitude. Le Chat, Issautier, and Meyer-Vernet ([2012](#)) considered the data from *Helios*, *Uysses* and *Wind* spacecraft and concluded that the energy flux of the solar wind is independent on latitude and varies weakly with the solar cycle. Thus there are many observational confirmations that there is a kind of invariance $nV^q = \text{const}$, where $q \geqslant 2$ for the solar wind parameter in the inner heliosphere, but still no fundamental theoretical reasons for that have been found. More detailed investigations should be done in order to find the direct links between the solar activity in the corona and the solar wind parameters further in the heliosphere.

Let us discuss an observed difference in the solar wind mass flux latitudinal dependence between solar maxima of Solar Cycles 23 and 24. We suppose that this difference can also be connected with distribution of the coronal holes. Namely, the previous solar maximum (2001–2003) was characterized by large polar coronal holes and small equatorial ones. But the most recent solar maximum (2013–2015) has been characterized by weaker polar holes accompanied by relatively pronounced equatorial holes (Lowder, Qiu, and Leamon, [2017](#)). Therefore in terms of the solar wind mass flux this leads to a weaker dependence on the heliolatitude and less separation between maxima at middle latitudes.

Both SWAN data and the WSA-Enlil model show that in 2014 the solar wind mass flux has a well defined maximum at the north hemisphere (latitudes about $30-50°$) and much weaker maximum at the south hemisphere. This could be explained if the equatorial coronal holes at this period are shifted to the south hemisphere that would results in increase of the solar wind velocity and corresponding decrease of the mass flux. Unfortunately, we did not find observational confirmation of such behavior of the coronal holes. However, (Lowder, Qiu, and Leamon, [2017](#)) have shown that the sunspot distribution in 2013–2014 is asymmetric relative to the equator. Namely, at this time period sunspots are located at low latitudes and the southern hemisphere contains much more of them. The distribution of sunspots correlates with the distribution of active regions and solar flares (McIntosh *et al.*, [2015](#)), which also could be source of the fast solar wind. This could partially explain the behavior found of the solar wind mass flux.

Disclosure of potential conflicts of interest The authors declare that they have no conflicts of interest.

Publisher's Note   Springer Nature remains neutral with regard to jurisdictional claims in published maps and institutional affiliations.

References

Arge, C.N., Pizzo, V.J.: 2000, *J. Geophys. Res.* **105**, 10465. DOI.

Arge, C.N., Odstrcil, D., Pizzo, V.J., Mayer, L.R.: 2003, *Solar Wind Ten* **679**, 190. DOI.

Bemporad, A.: 2017, *Astrophys. J.* **846**, 86. DOI.

Bertaux, J.L., Kyrölä, E., Quémerais, E., Pellinen, R., Lallement, R., Schmidt, W., Berthé, M., Dimarellis, E., Goutail, J.P., Taulemesse, C., Bernard, C., Leppelmeier, G., Summanen, T., Hannula, H., Huomo, H., Kehlä, V., Korpela, S., Leppälä, K., Strömmer, E., Torsti, J., Viherkanto, K., Hochedez, J.F., Chretiennot, G., Peyroux, R., Holzer, T. (eds.): 1995, *Solar Phys.* **162**, 403. DOI.

Bruno, R., Villante, U., Bavassano, B., Schwenn, R., Mariani, F.: 1986, *Solar Phys.* **104**, 431. DOI.

Ebert, R.W., McComas, D.J., Elliott, H.A., Forsyth, R.J., Gosling, J.T.: 2009, *J. Geophys. Res.* **114**, A01109. DOI.

Gringauz, K.I., Bezrokikh, V.V., Ozerov, V.D., Rybchinskii, R.E.: 1960, *Sov. Phys. Dokl.* **5**, 361. ADS.

Hundhausen, A.J., Bame, S.J., Asbridge, J.R., Sydoriak, S.J.: 1970, *J. Geophys. Res.* **75**, 4643. DOI.

Izmodenov, V.V., Alexashov, D.B.: 2015, *Astrophys. J. Suppl. Ser.* **220**, 32. DOI.

Izmodenov, V.V., Katushkina, O.A., Quémerais, E., Bzowski, M.: 2013, *Cross-Calibration of Far UV Spectra of Solar System Objects and the Heliosphere* 7. DOI.

Jian, L.K., MacNeice, P., Taktakishvili, A., Odstrcil, D., Jackson, B., Yu, H.-S., Riley, P., Sokolov, I.: 2015, *Space Weather* **13**, 316. DOI.

Jian, L.K., MacNeice, P., Mays, M.L., Taktakishvili, A., Odstrcil, D., Jackson, B., Yu, H.-S., Riley, P., Sokolov, I.: 2016, *Space Weather* **14**, 592. DOI.

Joselyn, J.A., Holzer, T.E.: 1975, *J. Geophys. Res.* **80**, 903. DOI.

Katushkina, O.A., Izmodenov, V.V., Quemerais, E., Sokół, J.M.: 2013, *J. Geophys. Res.* **118**, 2800. DOI.

Katushkina, O.A., Izmodenov, V.V., Alexashov, D.B., Schwadron, N.A., McComas, D.J.: 2015, *Astrophys. J. Suppl. Ser.* **220**, 33. DOI.

King, J.H., Papitashvili, N.E.: 2005, *J. Geophys. Res.* **110**, A02104. DOI.

Kramar, M., Jones, S., Davila, J., Inhester, B., Mierla, M.: 2009, *Solar Phys.* **259**, 109. DOI.

Kramar, M., Airapetian, V., Lin, H.: 2016, *Front. Astron. Space Sci.* **3**, 25. DOI.

Lallement, R., Bertaux, J.L., Kurt, V.G.: 1985a, *J. Geophys. Res.* **90**, 1413. DOI.

Lallement, R., Bertaux, J.L., Dalaudier, F.: 1985b, *Astron. Astrophys.* **150**, 21. ADS.

Lallement, R., Quémerais, E., Koutroumpa, D., Bertaux, J.-L., Ferron, S., Schmidt, W., Lamy, P.: 2010, *Twelfth International Solar Wind Conference* **1216**, 555. DOI.

Lamy, P., Barlyaeva, T., Llebaria, A., Floyd, O.: 2014, *J. Geophys. Res.* **119**, 47. DOI.

Lamy, P., Floyd, O., Quémerais, E., Boclet, B., Ferron, S.: 2017, *J. Geophys. Res.* **122**, 50. DOI.

Le Chat, G., Issautier, K., Meyer-Vernet, N.: 2012, *Solar Phys.* **279**, 197. DOI.

Lindsay, B.G., Stebbings, R.F.: 2005, *J. Geophys. Res.* **110**, A12213. DOI.

Lowder, C., Qiu, J., Leamon, R.: 2017, *Solar Phys.* **292**, 18. DOI.

McComas, D.J., Barraclough, B.L., Funsten, H.O., Gosling, J.T., Santiago-Muñoz, E., Skoug, R.M., Goldstein, B.E., Neugebauer, M., Riley, P., Balogh, A.: 2000, *J. Geophys. Res.* **105**, 10419. DOI.

McComas, D.J., Elliott, H.A., Gosling, J.T., Reisenfeld, D.B., Skoug, R.M., Goldstein, B.E., Neugebauer, M., Balogh, A.: 2002, *Geophys. Res. Lett.* **29**, 1290. DOI.

McComas, D.J.: 2003, *Solar Wind Ten* **679**, 33. DOI.

McComas, D.J., Elliott, H.A., Gosling, J.T., Skoug, R.M.: 2006, *Geophys. Res. Lett.* **33**, L09102. DOI.

McComas, D.J., Ebert, R.W., Elliott, H.A., Goldstein, B.E., Gosling, J.T., Schwadron, N.A., Skoug, R.M.: 2008, *Geophys. Res. Lett.* **35**, L18103. DOI.

McComas, D.J., Angold, N., Elliott, H.A., Livadiotis, G., Schwadron, N.A., Skoug, R.M., Smith, C.W.: 2013, *Astrophys. J.* **779**, 2. DOI.

McIntosh, S.W., Leamon, R.J., Krista, L.D., Title, A.M., Hudson, H.S., Riley, P., Harder, J.W., Kopp, G., Snow, M., Woods, T.N., Kasper, J.C., Stevens, M.L., Ulrich, R.K.: 2015, *Nat. Commun.* **6**, 6491. DOI.

Meier, R.R.: 1977, *Astron. Astrophys.* **55**, 211. ADS.

Neugebauer, M., Snyder, C.W.: 1962, *Science* **138**, 1095. DOI.

Neugebauer, M., Snyder, C.W.: 1966, *J. Geophys. Res.* **71**, 4469. DOI.

Odstrcil, D.: 2003, *Adv. Space Res.* **32**, 497. DOI.

Parker, E.N.: 1958, *Astrophys. J.* **128**, 664. DOI.

Pizzo, V., Millward, G., Parsons, A., Biesecker, D., Hill, S., Odstrcil, D.: 2011, *Space Weather* **9**, S03004. DOI.

Quémerais, E., Izmodenov, V.: 2002, *Astron. Astrophys.* **396**, 269. DOI.

Quémerais, E., Lamy, P.: 2002, *Astron. Astrophys.* **393**, 295. DOI.

Quémerais, E., Lallement, R., Ferron, S., Koutroumpa, D., Bertaux, J.-L., KyröLä, E., Schmidt, W.: 2006, *J. Geophys. Res.* **111**, A09114. DOI.

Schwenn, R.: 2006, *Space Sci. Rev.* **124**, 51. DOI.

Steinitz, R.: 1983, *Solar Phys.* **83**, 379. DOI.

Steinitz, R., Eyni, M.: 1980, *Astrophys. J.* **241**, 417. DOI.

Tokumaru, M., Kojima, M., Fujiki, K.: 2012, *J. Geophys. Res.* **117**, A06108. DOI.

Wu, F.M., Judge, D.L.: 1979, *Astrophys. J.* **231**, 594. DOI.